



Cite this: *Soft Matter*, 2018, 14, 8828

An analytic model of two-level compressive buckling with applications in the assembly of free-standing 3D mesostructures

Yan Shi,^{†ab} Pengyu Pei,^{†a} Xu Cheng,^b Zheng Yan,^c Mengdi Han,^d Zhi Li,^a Cunfa Gao,^a John A. Rogers,^{de} Yonggang Huang^{df} and Yihui Zhang^{ib* b}

Recently developed methods for mechanically-guided assembly exploit stress release in prestretched elastomeric substrates to guide the controlled formation of complex three-dimensional (3D) mesostructures in advanced functional materials and integrated electronic devices. The techniques of interfacial photopolymerization allow for realization of such 3D mesostructures in free-standing forms, separated from their elastomeric substrate, *via* formation of an integrated base layer. Theoretical models for the complex modes of deformation associated with this scheme are essential in the optimal design of the process parameters. Here, we present an analytic finite-deformation model of an isolated double-ribbon structure to describe the buckling process and morphology change of the assembled mesostructures upon removal of the substrate. As validated by finite element analyses (FEA), this analytic model can accurately predict the profiles of the double-ribbon structure with a range of different design parameters. We further illustrate the extension of this model to the analyses of 3D mesostructures with different geometries. Inspired by analytic results for flexible base structures, combined experimental results and numerical simulations demonstrate that mechanical interactions between the two different layers can be leveraged to achieve hierarchical assembly of 3D mesostructures. These findings could be useful in further advances in designs of free-standing 3D mesostructures based on mechanically-guided assembly.

Received 26th August 2018,
Accepted 15th October 2018

DOI: 10.1039/c8sm01753k

rsc.li/soft-matter-journal

1. Introduction

Techniques for the formation of three-dimensional (3D) mesostructures are of rapidly growing interest in many fields of study, particularly those that involve emerging technologies in biomedicine,^{1–3} robotics,^{4–9} batteries,^{10,11} sensors,^{9,12,13} micro-electro-mechanical systems (MEMS),^{14,15} optics and

optoelectronics.^{16–20} Existing approaches include printing-type techniques (*e.g.*, two/multi-photon lithography,^{20,21} direct writing,^{22–24} 3D printing^{2,25}), folding/bending-type techniques (*e.g.*, *via* residual stress,^{26,27} capillary force,^{28,29} active materials^{30,31}), and mechanically-guided assembly techniques (*e.g.*, *via* compressive buckling,^{24,32–34} tensile buckling³⁵). This third category of methods offers unique capabilities in the formation of complex 3D mesostructures in high-performance electronic materials and integrated devices, due to its compatibility with well-developed technologies in modern industries.^{32,33,36–44} These techniques also apply over a wide range of length scales.^{34,36} Here, an elastomeric substrate serves as an assembly platform that applies forces to a 2D micro/nano-scale precursor structure to affect its transformation into a controlled 3D architecture. In most cases, the elastomeric substrate must remain to hold the 3D architectures in their desired forms. This requirement poses certain limitations in practical applications that require, as examples, high temperature operation or precise dimensional stability. By introducing a series of steps in photolithography and planar processing, Yan *et al.*⁴⁵ recently reported strategies that involve the integration of a photodefinable polymer (epoxy; SU8) layer as an integrated base that allows release of 3D structures from their elastomeric substrate. The pattern and thickness of

^a State Key Laboratory of Mechanics and Control of Mechanical Structures, Nanjing University of Aeronautics & Astronautics, Nanjing 210016, China

^b Center for Flexible Electronics Technology, Center for Mechanics and Materials, AML, Department of Engineering Mechanics, Tsinghua University, Beijing 100084, P. R. China. E-mail: yihuizhang@tsinghua.edu.cn

^c Departments of Biomedical, Biological & Chemical Engineering, Mechanical & Aerospace Engineering, University of Missouri, Columbia, MO 65211, USA

^d Center for Bio-Integrated Electronics, Northwestern University, Evanston, IL 60208, USA

^e Departments of Materials Science and Engineering, Biomedical Engineering, Neurological Surgery, Chemistry, Mechanical Engineering, Electrical Engineering and Computer Science, and Simpson Querrey Institute for BioNanotechnology, Northwestern University, Evanston, Illinois 60208, USA

^f Departments of Civil and Environmental Engineering, Mechanical Engineering and Materials Science and Engineering, Northwestern University, Evanston, IL 60208, USA

[†] These authors contributed equally to this work.

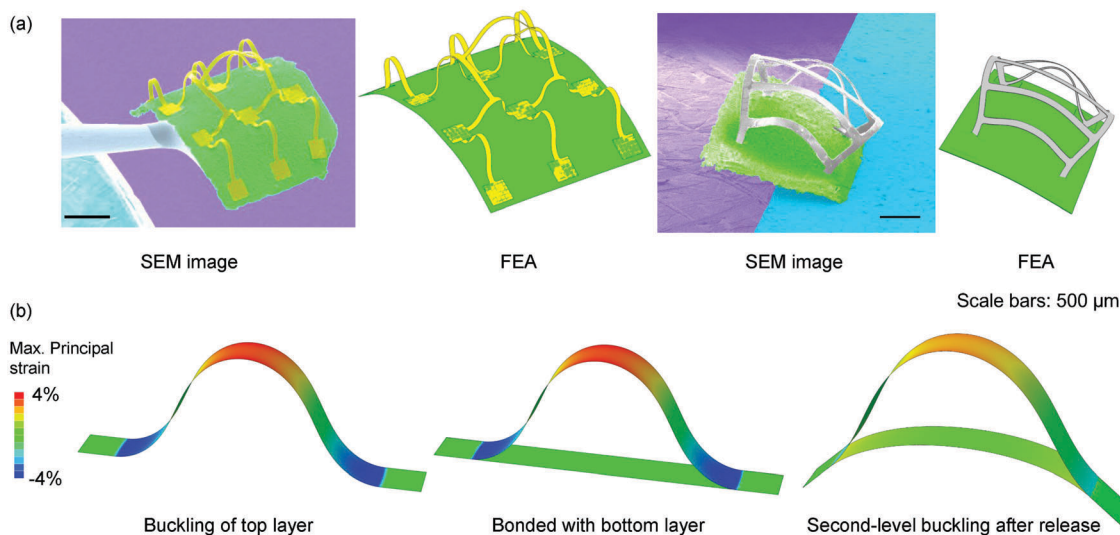


Fig. 1 (a) Scanning electron microscope (SEM) images and finite element analysis (FEA) of isolated network and peacock-like structures formed through mechanically-guided assembly. (b) FEA results that illustrate the two-level buckling process for the assembly of an isolated double-ribbon structure. Scale bars, 500 μm. (a) is adapted with permission from Yan *et al.* (ref. 44), Copyright (2017), National Academy of Sciences.

the base layer can be modified by choosing different processing parameters (*e.g.*, dose of ultraviolet (UV) exposure, duration of post expose bake) and photomasks for control of exposure to UV light. Fig. 1(a) shows scanning electron microscope (SEM) images and simulation results of a free-standing network and a peacock-like structure formed in this way.⁴⁵ Both experiments and simulations show that a base with a sufficiently large bending stiffness (*e.g.*, more than ten times larger than that of the top 3D structure) can maintain the shape of the 3D mesostructure (*e.g.*, the right panel of Fig. 1(a)). Bases with insufficiently large bending stiffnesses tend to deform with the 3D mesostructure (*e.g.*, the left panel of Fig. 1(a)) after the release. The bending deformations of the base layer mainly result from residual stresses restored in the buckled mesostructures, and this procedure can be regarded as a two-level buckling process. An understanding of such a two-level buckling phenomenon is essential for optimal design of processing parameters related to this approach. Although many theoretical models exist for postbuckling behavior in thin-film structures,^{19,46–49} they focus mainly on the single process of compressive buckling and cannot be used directly to analyze the above two-level buckling process that involves an additional process of energy conversion from the top 3D structure to the base structure.

In this work, we developed an analytic model to predict the deformations of a two-level buckling process in a double-ribbon structure (shown in Fig. 1(b)), which can be extended to the analyses of more complex 3D structures. Such a double-ribbon structure (Fig. 1(b)) represents a degenerated 2D model that illustrates the two-level buckling process for the assembly of free-standing 3D mesostructures. Specifically, an arch-shaped, top-layer ribbon was firstly formed through the compressive buckling of a straight 2D precursor, with use of a prestretched soft substrate (which is not shown in Fig. 1(b)). Then, *via* backside UV light treatment, a bottom-layer ribbon in photo-definable polymer (SU8) was generated, with terminals bonded with the top-layer ribbon. Release of the ribbons from the

substrate induces bending of the bottom-layer ribbon, leading to the formation of a free-standing double-ribbon structure. As validated by finite element analyses (FEA), the developed model suggests a significant role of the stiffness ratio between the top and bottom layers in the two-level buckling process. By utilizing this type of two-level buckling approach, we demonstrated hierarchical assembly of complex 3D mesostructures in free-standing forms, through combined FEA and experimental studies.

2. An analytic model of the two-level buckling

Fig. 2 provides a schematic illustration of the mechanics model for the double-ribbon structure. For slender ribbon structures with the thickness-to-length ratio smaller than 0.1, we adopted the Euler beam theory to model the deformations, neglecting the effects of axial elongation (*i.e.*, related to the membrane strain) and shear deformations of the ribbons. The top-layer ribbon with an original length of L_1 and bending stiffness of $E_1 I_1$ (E , Young's modulus; I , moment of inertia) is clamped at the two ends. With the left end fixed, the right end moves left to apply a compressive force (p) to the ribbon structure, triggering the compressive buckling when the force reaches a critical value. For simplicity, the length of the bonding sites was neglected in the current model. According to the initial postbuckling analyses of a single straight ribbon,⁴⁶ the profile of the buckled structure can be given as

$$U_{1,2} = a \sin^2 \frac{\pi x}{L_1}, \quad (1)$$

where U represents the coordinate of the profile, with the origin point fixed at the left end of the ribbon; the first subscript denotes the ribbon number and the second one denotes the coordinate direction. Here, $U_{1,2}$ means the position of the top-layer ribbon along y axis, and a is the amplitude of the buckled configuration, depending on the level of compressive loading. During the

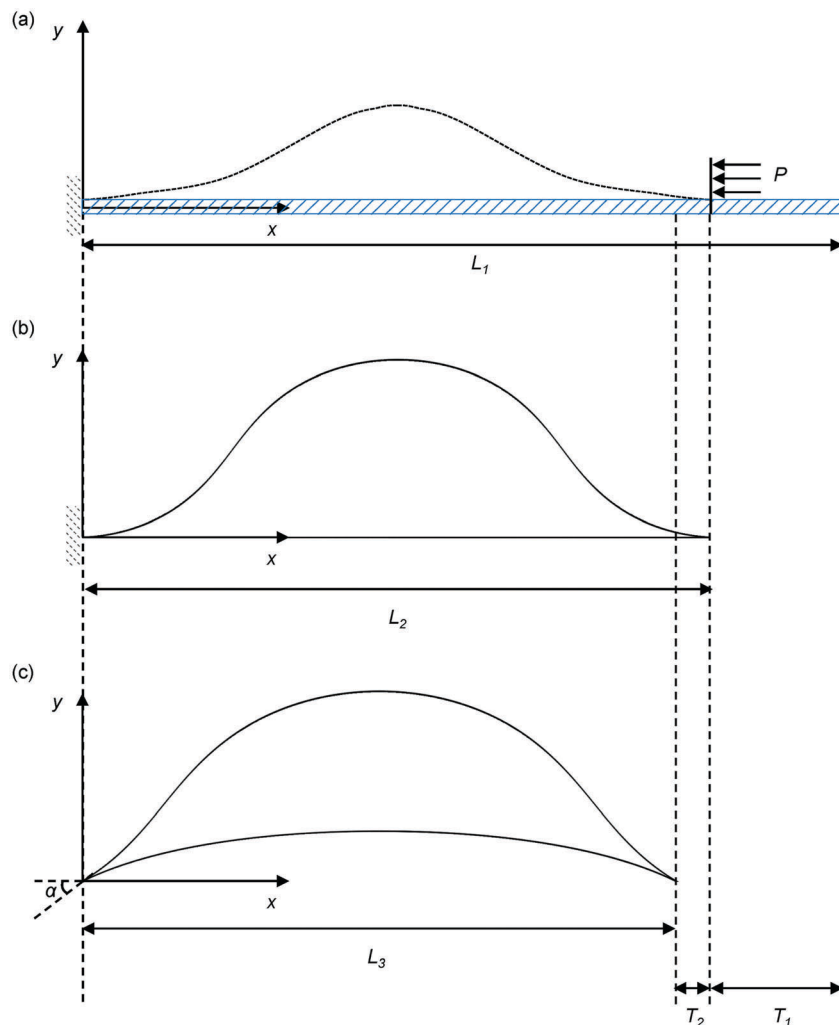


Fig. 2 Schematic illustrations of the buckling procedures of the double-ribbon structure studied in the analytic model. (a) Front view of a clamped straight ribbon with compressive load applied at the right end. The buckling mode is described using the dashed line. (b) A bottom-layer ribbon developed aligned to the buckled top-layer one, with both ends bonded together. (c) Illustration of the deformed configuration due to the 2nd-level buckling upon load release.

postbuckling, the total axial load p is $\dot{p} + \bar{p}$, where \bar{p} represents the additional axial load beyond the critical buckling, which is given by⁴⁶

$$\bar{p} = \frac{\pi^2 a^2}{8L_1^2} \frac{1 - 3\frac{\dot{p}}{E_1 A_1}}{1 - \frac{\dot{p}}{E_1 A_1}} \dot{p}, \quad (2)$$

and \dot{p} is the Euler critical load and is expressed as $\dot{p} \approx \frac{4\pi^2 E_1 I_1}{L_1^2}$ for the ends-fixed ribbon, as analyzed herein. Here, A_1 is the cross-section area of the ribbon. Based on the assumption of negligible axial elongation, we have $\frac{1 - 3\frac{\dot{p}}{E_1 A_1}}{1 - \frac{\dot{p}}{E_1 A_1}} \approx 1$. Then the amplitude is obtained from eqn (2) as

$$a \approx L_1 \sqrt{\frac{8\bar{p}}{\pi^2 \dot{p}}}, \quad (3)$$

For the ends-fixed ribbon, the axial displacement $U_{1,1}$ can be approximated by⁴⁶

$$U_{1,1} \approx \frac{\pi a^2}{16L_1} \left(\sin \frac{4\pi x}{L_1} - \frac{4\pi x}{L_1} \right) \quad (0 \leq x \leq L_1), \quad (4)$$

Thereby, the axial compression T_1 can be expressed by,

$$T_1 = -U_{1,1}|_{x=L_1} \approx \frac{\pi^2 a^2}{4L_1}. \quad (5)$$

For the guided assembly of 3D structures through compressive buckling, the compressive strain (or distance) is usually controlled by a mechanical stretcher, which also represents an important tunable parameter for manipulating the configurations of the structure. For a given axial compression T_1 , the amplitude a can be determined by eqn (5) as $a = \frac{2\sqrt{L_1 T_1}}{\pi}$. Then the profile of the buckled ribbon in eqn (1) can be described analytically.

As shown in Fig. 2(b), a new bottom-layer ribbon was developed after the compressive buckling of the top-layer ribbon, and they were bonded together at the two ends. The original length of the bottom-layer ribbon is

$$L_2 = L_1 - T_1. \quad (6)$$

After the removal of the elastomeric substrate, the clamped boundaries were relaxed to allow rotational motions at the two ends, while the rotational angles of the two different layers are the same during the deformations. FEA results show that the profiles of the buckled ribbons can be well characterized by trigonometric functions or their variants as,

$$U_{1,2}^* = A_1 \sin \frac{\pi x}{L_3} + A_2 \sin^2 \frac{\pi x}{L_3} \quad (0 \leq x \leq L_3), \quad (7)$$

$$U_{2,2}^* = A_3 \sin \frac{\pi x}{L_3} \quad (0 \leq x \leq L_3). \quad (8)$$

It is noteworthy that the linear term of sinusoidal function is typically chosen to describe the configuration of a buckled ribbon with simply supported ends, while the quadratic term is widely used to capture the buckled configuration in the condition of clamped ends. In the current analyses, the ends of the top-layer ribbon are bonded onto the base structure that imposes a finite constraint on the rotation. As such, the boundary constraint can be regarded as an intermediate state between simply supported and clamped conditions. The FEA results also indicate that the displacement of the top-layer ribbon can be well treated as a combination of the linear and quadratic terms. Furthermore, with consideration of the numbers of equations and unknowns, we simply used a linear term (eqn (8)) to characterize the displacement of the bottom-layer ribbon. Similar displacement functions were also adopted in previous postbuckling analyses.^{39,47,48} In eqn (7) and (8), the superscript “*” denotes the displacement in the final condition, *i.e.*, after the removal of the substrate. L_3 represents the axial projection length of both layers (shown in Fig. 2(c)). A_1 , A_2 and A_3 are the unknown parameters to be determined. During the manufacturing process, the top-layer and bottom-layer ribbons are bonded perfectly at small regions adjacent to the two ends. Therefore, the slopes of the two ribbons are approximately the same at the ends, which requires the rotational angle (α in Fig. 2(c)) to be the same for the two layers, *i.e.*,

$$\left. \frac{dU_{1,2}^*}{dx} \right|_{x=0} = \left. \frac{dU_{2,2}^*}{dx} \right|_{x=0}, \quad (9)$$

All the unknown parameters (A_1 , A_2 , A_3 and L_3) can be determined by eqn (9), the invariant arc lengths of the ribbons as well as the energy conservation detailed below.

For the ultra-thin ribbons, the membrane strain resulted from the axial elongation or shrinkage was usually negligible, as compared to the bending-induced strain (at the top and bottom surfaces) during the compressive buckling, since the bending deformations are more energy favorable.^{47,50} As such, the axial elongation/shrinkage of the ribbons can be neglected,

and therefore, the total arc lengths of the two ribbons remain unchanged during the deformation, requiring that

$$\int_0^{L_3} \sqrt{1 + [(U_{1,2}^*)']^2} dx = L_1, \quad (10)$$

$$\int_0^{L_3} \sqrt{1 + [(U_{2,2}^*)']^2} dx = L_2. \quad (11)$$

During the first-level buckling process, the work done by the external force converts into the deformation energy that consists of the membrane energy and the bending energy. By neglecting the membrane strain, the deformation energy is equal to the bending energy. The external work W_{ex} can be derived from $p = \dot{p} + \bar{p}$, and eqn (3) and (5),

$$W_{\text{ex}} = \int_0^{T_1} p ds = \int_0^{T_1} \left(1 + \frac{T_1}{2L_1} \right) \dot{p} ds = \left(T_1 + \frac{T_1^2}{4L_1} \right) \dot{p} \quad (12)$$

in the condition shown in Fig. 2(a). From eqn (7) and (8), the bending energy at the final state shown in Fig. 2(c) can be expressed as

$$W_{\text{final}} = \int_0^{L_3} \frac{E_1 I_1 \frac{[(U_{1,2}^*)'']^2}{[1 + ((U_{1,2}^*)')^2]^3} + E_2 I_2 \frac{[(U_{2,2}^*)'']^2}{[1 + ((U_{2,2}^*)')^2]^3}}{2} dx. \quad (13)$$

where the subscripts “1” and “2” represent the properties for the top and bottom layers, respectively. The energy conservation of the system requires

$$W_{\text{ex}} = W_{\text{final}}. \quad (14)$$

Based on eqn (9)–(14), the unknown parameters A_1 , A_2 , A_3 and L_3 can be determined. The profile of the double-ribbon structure was then obtained accordingly. The compression of the bottom-layer ribbon along the axial direction can be calculated from $T_2 = L_2 - L_3$.

3. Effects of the bending stiffness ratio on the structural change

3.1 Validation of the analytic model

In this section, 3D FEA were employed to validate the above analytic model. In FEA, four-node shell elements were adopted to model the ribbons. The effective length (L_1) and width of the top-layer ribbon were 1 mm and 0.1 mm, and square bonding sites (0.1 mm by 0.1 mm) were assigned at each end of the layer for bonding to the bottom-layer ribbon. The entire simulation consists of three main steps. Firstly, the critical buckling strain and corresponding buckling mode determined from linear buckling analysis were implemented as an initial imperfection in the postbuckling calculations to model the deformed shape of the top-layer ribbon at different levels of compression, *e.g.*, 20% and 30% compressive strain. Secondly, a bottom-layer ribbon was built with the same width and set to bond with

the top-layer ribbon during the subsequent deformations. It is noteworthy that the displacement loads applied to the top layer were maintained during this procedure. Finally, the removal of the displacement loads relaxes the structure to an equilibrium state. The simulations of the two-level buckling process were performed using the conventional static analysis in the commercial software ABAQUS, and the convergence of mesh sizes was tested to ensure computational accuracy. SU8 was adopted as the top-layer material and its elastic modulus (E_1) and Poisson's ratio (ν) are $E_1 = 4.02$ GPa and $\nu_1 = 0.22$,⁴⁵ respectively. According to the analytic model, the bending stiffness ratio (E_2I_2/E_1I_1) is essential in the determination of the final configurations. In the current FEA, the thicknesses of the top and bottom ribbons are both set to 0.01 mm for simplicity, and the variation of the bending stiffness ratio is realized by varying the Young's modulus of the bottom ribbon.

Fig. 3 shows the profiles of the top-layer and bottom-layer ribbons predicted by both the analytic model (dots) and FEA (line). Here, two different levels of compressive strains, 20% (black) and 30% (red), were used to form the arc-shaped top ribbon through the buckling-guided assembly. The bending stiffness ratio (E_2I_2/E_1I_1) ranges from 2 in Fig. 3(a) to 20 in Fig. 3(d). As expected, the bottom-layer ribbon with a larger bending stiffness tends to maintain the as-assembled shape of the top-layer. This is evidenced by both the amplitude of the bottom-layer (A_3) and the compressed length (T_2) that decreases with increasing the bending stiffness ratio (E_2I_2/E_1I_1). In all of the different cases, the profiles predicted by the analytic model agree well with the FEA results. The relative large discrepancy at lower bending stiffness ratios are mainly attributed to the simplified displacement function (*i.e.*, using a linear sinusoidal term) that is not able to characterize the deformation of the bottom-layer ribbon in this regime.

Aside from the final 3D configuration, the overall variation of the mesostructure geometry also represents an important concern of the morphological control during the fabrication. For the double-ribbon structure, two dimensionless parameters, *i.e.*, the average deflection ratio (\bar{A}_3/L_1 , with \bar{A}_3 denoting the average displacement along the y direction) and compressed length ratio (T_2/L_1) of the bottom layer characterize the structural variation in a quantitative manner. \bar{A}_3/L_1 measures the flatness of the base ribbon structure, which is important in the mechanically-guided 3D assembly. T_2/L_1 provides a quantitative measurement of the in-plane compression (along the x direction) after the relaxation of the entire structure. Smaller average deflection ratio or shorter compressed length ratio indicate a lower level of morphology change in the top-layer ribbon, which is more preferable in the assembly of free-standing 3D mesostructures. Fig. 4 presents the results of these two parameters (\bar{A}_3/L_1 and T_2/L_1) for a wide range of bending stiffness ratios, with consideration of two typical compressive strains (20% and 30%) in the first-level buckling. Both parameters decrease rapidly with increasing the bending stiffness ratio, which is consistent with the results in Fig. 3. For a bending stiffness ratio over 20, the deformations of the top-layer ribbon are basically negligible during the 2nd level buckling, *i.e.*, after the removal of the substrate.

3.2 Extension of the analytic model

The above analytic model can be extended directly to the analyses of some 3D mesostructures. One of the examples is a double cross-ribbon structure (with same widths) assembled through bi-directional buckling. Fig. 5(a and b) shows the configurations of the double cross-ribbon structure with two different bending stiffness ratios (1 and 10) and bi-axial compressive strains (20% and 30%) used to assemble the cross-ribbon

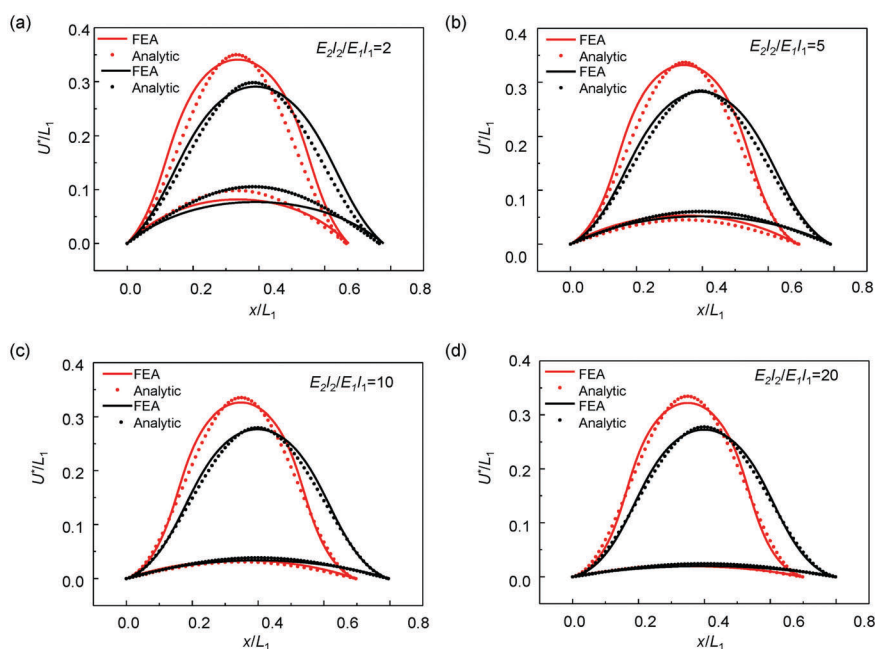


Fig. 3 Profiles of the top-layer and bottom-layer ribbons predicted by the analytic model (dots) and FEA (lines), where 20% (black) and 30% (red) compressions are adopted for the 1st-level buckling. The bending-stiffness ratio is set as 2, 5, 10 and 20 in (a), (b), (c) and (d), respectively.

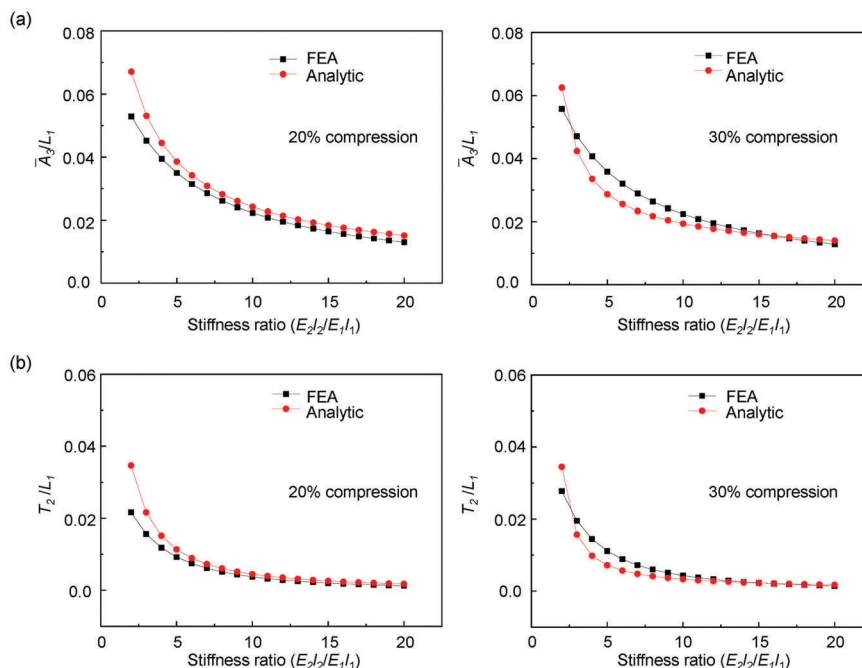


Fig. 4 Overall deformations of the double-ribbon structure calculated with FEA (black) and analytic model (red), respectively. (a) Average deflection ratio (\bar{A}_3/L_1) versus bending-stiffness ratio in the conditions of 20% and 30% initial compressions, respectively. (b) Axial compression ratio (T_2/L_1) of the bottom-layer ribbon versus bending-stiffness ratio in the conditions of 20% and 30% initial compressions, respectively.

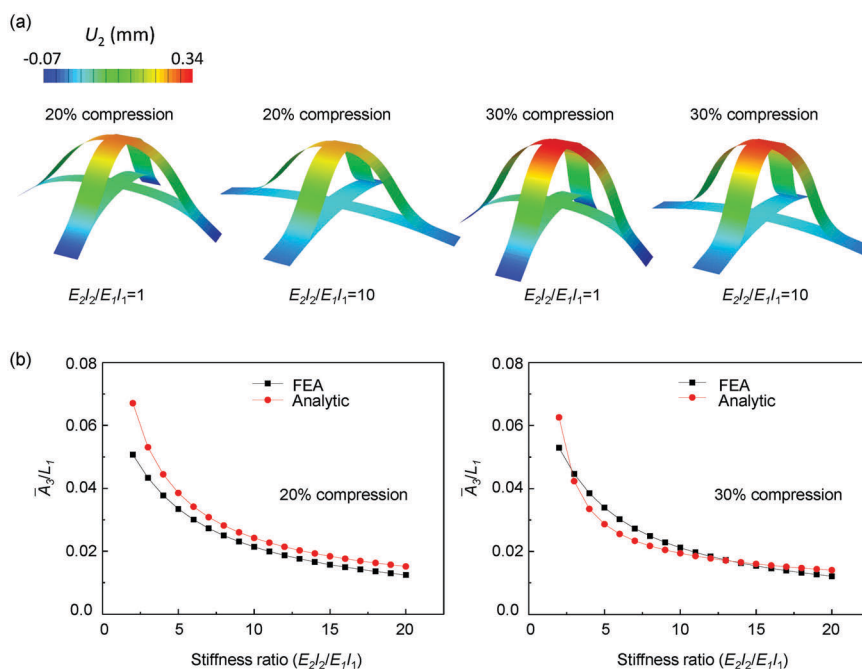


Fig. 5 Simulation results for the assembly of hierarchical structures by cross-shaped ribbons. (a) Configurations of the buckled structures with two different initial compressions (20% and 30%) and stiffness ratios (1 and 10). (b) Average deflections ratios calculated with FEA (black) and analytic model (red) in the conditions of 20% and 30% initial compressions, respectively.

structure in the 1st level buckling. The predictions of the deflection ratio based on the analytic model show good accordance with the FEA (Fig. 5(b)), indicating that this model can be well generalized to the analyses of 3D beam structures with

bidirectional symmetry or multi-fold rotational symmetry. This model is also applicable to the double-ribbon structure with different widths for the two layers, considering the proportional dependence of the bending stiffness on the ribbon width.

For the design of more complex 3D mesostructure with patterned bases, the concept of equivalent bending stiffness can be employed, and the ratio $(E_2 t_2^3 / E_1 t_1^3)$ can be regarded as a more general parameter to govern the process, where t_2 and t_1 are the thicknesses of two layers.

As mentioned above, a stiffer base (bottom-layer ribbon) is preferable in fixing the shape of the isolated 3D structure. From another perspective, a more flexible base (or a lower stiffness ratio) results in a more evident deformation of the bottom layer, which offers a possible route to the assembly of complex 3D structures. The theoretical analyses in Section 3.1 suggest a bending stiffness ratio $(E_2 I_2 / E_1 I_1)$ less than 5 can induce a distinct deformation of the bottom-layer structure. Following this concept,

we introduced a base design inspired by Kirigami,^{32,38} an ancient art of paper cutting, to achieve 3D assembly of the bottom-layer structure, even when the structures at different layers have the same thicknesses. As an illustrative example, Fig. 6(a) presents a design, in which the bottom layer (blue) is cut into an unfolded 2D box-like shape, consisting of five membranes. Here, the narrowed regions whose widths are similar to those of the top-layer (green) serve as creases, connecting the different membranes. Due to the substantially reduced stiffness at the creases, the bending deformations of the bottom layer tend to localize at the narrowed regions, while the membranes remain almost flat in most cases. Based on this assumption and the analytic model in Section 2, the two-level buckling process of the 3D box-like

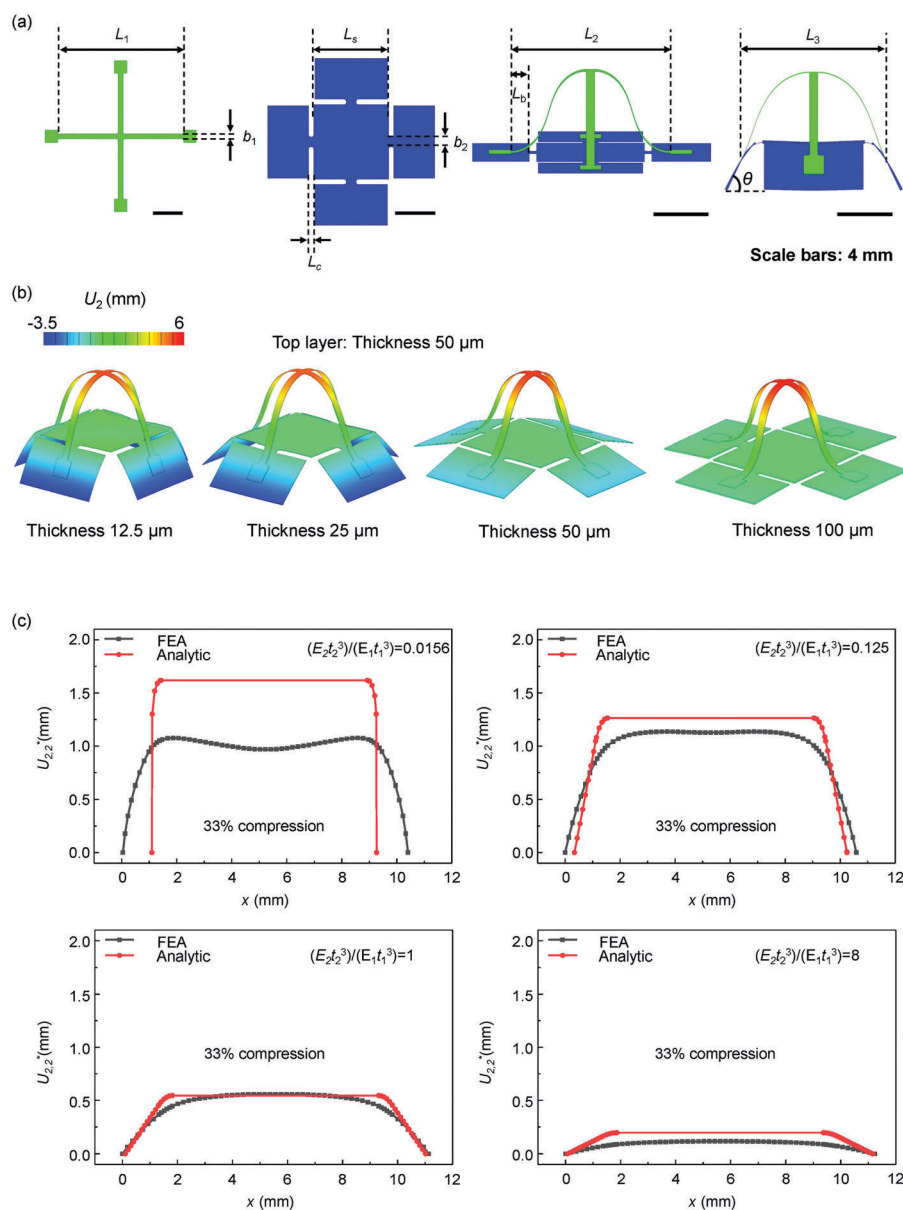


Fig. 6 Schematic illustration of the buckling process to form the 3D box-like structure. (a) Feature dimensions used in the analytic model. (b) Configurations of the buckled structures with the thickness ratio ranging from 0.25 to 2. (c) Profiles of the box-like structure predicted by FEA (black) and analytic model (red). The equivalent bending stiffness ratio is set as 0.0156, 0.125, 1 and 8, respectively. Scale bars, 4 mm.

structure (Fig. 6(a)) can be analyzed. The profile of the top structure in the 1st level buckling are given in eqn (1)–(5). The original length L_1 and width b_1 of the top layer are shown in Fig. 6(a). The deformation of the bottom layer is accommodated mainly by the creases (width, b_2). To simplify the analyses, the crease region is assumed to deform into a circular arc after the buckling process. Based on these assumptions, the profiles of the buckled ribbons and box can be characterized by

$$U_{1,2}^* = A_1 \sin \frac{\pi x}{L_3} \quad (0 \leq x \leq L_3), \quad (15)$$

$$U_{2,2}^*$$

$$= \begin{cases} x \tan \theta & (0 \leq x \leq L_b \cos(\theta)) \\ y_0 + \sqrt{R^2 - (x - x_0)^2} & (L_b \cos(\theta) < x < x_0) \\ y_0 + R & (x_0 \leq x \leq x_0 + L_s) \\ y_0 + \sqrt{R^2 - (x - (x_0 + L_s))^2} & (x_0 + L_s < x < L_3 - L_b \cos(\theta)) \\ (L_3 - x) \tan(\theta) & (L_3 - L_b \cos(\theta) \leq x \leq L_3) \end{cases}, \quad (16)$$

where L_s represents the side length of the central square and L_c is the length of the crease, as shown in Fig. 6(a). L_3 is the x -directional length between the bonding sites of the top structure in the final configuration. L_b is a feature size shown in Fig. 6(a). Note that $x_0 = L_b \cos(\theta) + R \sin(\theta)$, $y_0 = L_b \sin(\theta) - R \cos(\theta)$ and $R = L_c/\theta$ can be directly obtained from geometric relations. By neglecting the membrane energy, the unknowns A_1 , L_3 and θ can be obtained by substituting eqn (15) and (16) into eqn (10)–(14).

FEA were employed to validate this theoretical extension. In the simulations, the 2D patterns for the top-layer and bottom-layer structures are shown in Fig. 6(a). The thickness (t_1) for the top layer is 50 μm , while that (t_2) for the bottom layers ranges from 12.5 to 100 μm , as in Fig. 6(b). In other words, the general bending stiffness ratio ($E_2 t_2^3 / E_1 t_1^3$) ranges from 0.0156 to 8. The profiles of the box structure predicted by this analytic model and FEA are shown in Fig. 6(c), indicating that the analytic model derived from the 2D ribbons can be extended to the analyses of 3D box-like structure for moderate stiffness ratios (e.g., >0.1). For extremely small equivalent bending stiffness ratios ($E_2 t_2^3 / E_1 t_1^3$), e.g., 0.0156 in the first example of Fig. 6(c),

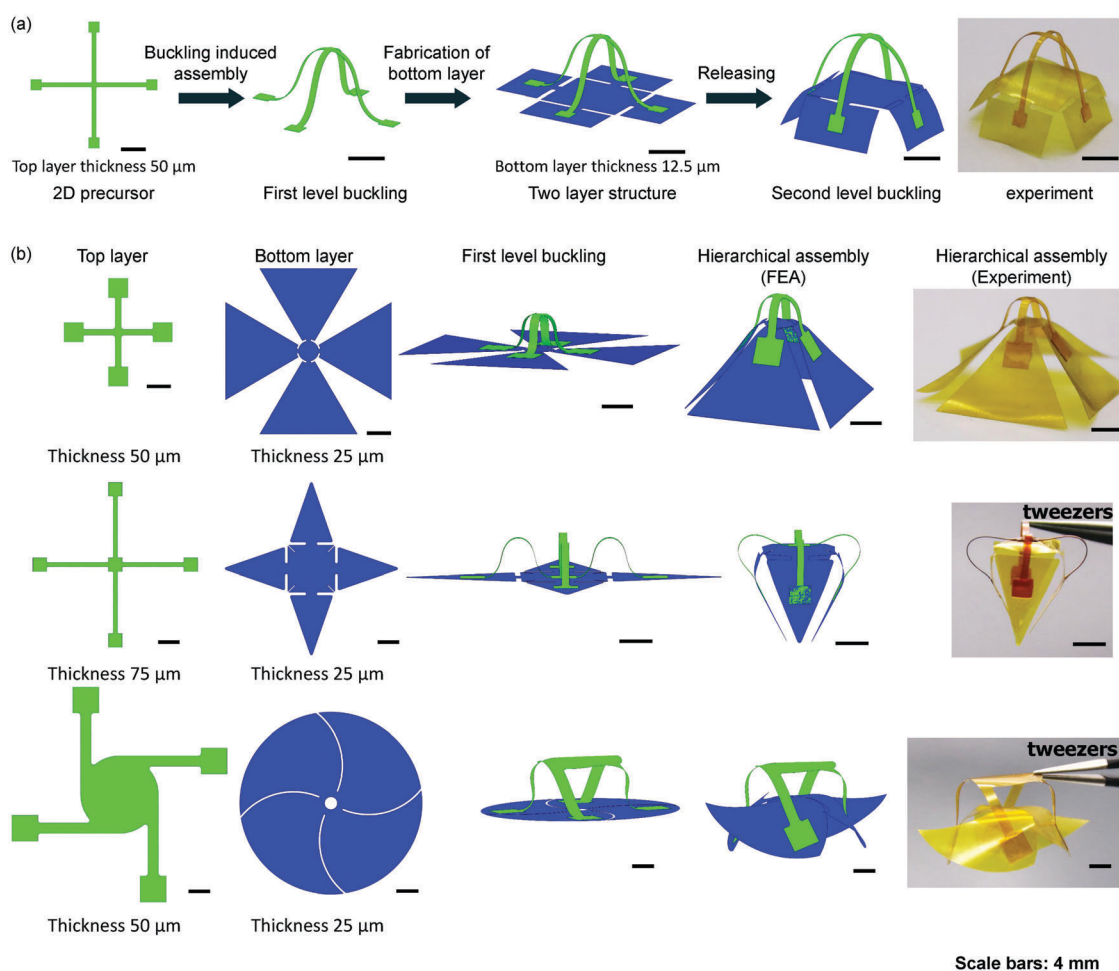


Fig. 7 Hierarchical assembly of complex 3D mesostructures. (a) Schematic illustration of an approach for forming 3D box-like structure via two-level buckling process, together with an experimental result. (b) 2D precursor designs and assembled configurations for mesostructures that resemble the pyramid, diamond and propeller. Scale bars, 4 mm.

a relative large discrepancy between the FEA and model occurs, since the crease regions are unable to accommodate all of the deformation energy. According to these derivations, it is noteworthy that the above model can be also extended to the analyses of other 3D structures that are assembled mainly by bending deformations.

4. Application in the hierarchical assembly of complex 3D mesostructures

Following the concepts described in Section 3.2, a novel approach for hierarchical assembly of 3D structures is presented in this section. As shown in Fig. 7(a), firstly, a planar precursor of the cross-like structure was partly bonded on a biaxially prestretched elastomeric substrate (not shown in figures),^{33,38} to allow the formation of 3D tent-like structure after relaxing the substrate. Secondly, a patterned box-like base (thinner than the top structure) was developed underneath the tent structure. Finally, after releasing from the substrate, the top-layer tent structure drives the reconfiguration of the patterned base into a 3D box structure without any further intervention.

Millimeter-scale experiments were carried out to demonstrate the utility of this approach in the hierarchical assembly. The 2D precursors of single-layer polyimide (PI) films (12.5, 25, 50, and 75 μm in thickness) were patterned into desired shapes by an automated mechanical cutting. For films thinner than 60 μm , a thermal release tape, whose adhesion reduces considerably after heating to 95 $^{\circ}\text{C}$, was utilized to facilitate the retrieval of the patterned films from the adhesive cutting mat. The assembly process started with the adhesion of the bottom layer to a water-soluble tape, whose adhesion reduces considerably after immersing in water. Next, the bonding sites of the buckled (top) structure are glued to the bottom layer with a commercial adhesive (Super Glue, Gorilla Glue Company), followed by curing for ~ 5 min at room temperature. Finally, the water-soluble tape with multilayered structure is immersed in water. After heating (80 $^{\circ}\text{C}$) for ~ 40 min, the multilayered structure fell off the tape, assembling into the desired hierarchical structure automatically. This process was also modeled quantitatively by FEA, in which the elastic modulus of 2.5 GPa and Poisson's ratio of 0.34 were used for the PI films.

Fig. 7 presents a set of complex 3D structures that resemble box, pyramid, diamond and propeller, as achieved using this approach. In all of the different designs, 33% biaxial compressive strain were used in the 1st level buckling to form the top-layer structures. To realize evident folding deformation in the bottom-layer structures, the top-layer structures are all thicker than the bottom layers in the different designs in Fig. 7. For such complex assembly processes, the FEA results still show good agreements with the experimental images for the final configurations, suggesting the FEA as a reliable design tool. These results well demonstrate the concepts of the hierarchical assembly, which can potentially scale down for the rapid formation of smaller mesostructures.

5. Concluding remarks

In summary, we developed an analytic model for the two-level buckling process in an isolated double-ribbon structure. The analytic results, as validated by FEA, provide a simple way to estimate the morphology change of the isolated structures after their release from the substrate. In the two-level buckling process, the material modulus and shell thickness come into play in the form of bending stiffness ratio, according to the quantitative results that characterize the shape fixity of the assembled structure (*i.e.*, the top-layer structure). The results show that the developed model can be extended to the analyses of more complex 3D mesostructures. In the condition of small bending stiffness ratios (*i.e.*, with relative flexible base structure), we leveraged the mechanical interactions between the two different layers to demonstrate a route to the hierarchical 3D self-assembly, by combined mechanics modeling and experimental measurement. This study can serve as references in the design of isolated 3D mesostructure and micro-devices.

Conflicts of interest

There are no conflicts of interest to declare.

Acknowledgements

Y. S. acknowledges the support from the National Natural Science Foundation of China (Grant No. 11702131). Y. Z. acknowledges the support from the National Natural Science Foundation of China (Grant No. 11672152 and 11722217), Thousand Young Talents Program of China and Tsinghua National Laboratory for Information Science and Technology.

References

- 1 L. Xu, S. R. Gutbrod, A. P. Bonifas, Y. Su, M. S. Sulkin, N. Lu, H. J. Chung, K. I. Jang, Z. Liu, M. Ying, C. Lu, R. C. Webb, J. S. Kim, J. I. Laughner, H. Cheng, Y. Liu, A. Ameen, J. W. Jeong, G. T. Kim, Y. Huang, I. R. Efimov and J. A. Rogers, *Nat. Commun.*, 2014, **5**, 3329.
- 2 J. U. Lind, T. A. Busbee, A. D. Valentine, F. S. Pasqualini, H. Yuan, M. Yadid, S.-J. Park, A. Kotikian, A. P. Nesmith, P. H. Campbell, J. J. Vlassak, J. A. Lewis and K. K. Parker, *Nat. Mater.*, 2017, **16**, 303–308.
- 3 D. H. Kim, N. S. Lu, Y. G. Huang and J. A. Rogers, *MRS Bull.*, 2012, **37**, 226–235.
- 4 M. Wehner, R. L. Truby, D. J. Fitzgerald, B. Mosadegh, G. M. Whitesides, J. A. Lewis and R. J. Wood, *Nature*, 2016, **536**, 451–455.
- 5 J. Wang and W. Gao, *ACS Nano*, 2012, **6**, 5745–5751.
- 6 N. S. Lu and D. H. Kim, *Soft Robot.*, 2014, **1**, 53–62.
- 7 B. Jin, H. Song, R. Jiang, J. Song, Q. Zhao and T. Xie, *Sci. Adv.*, 2018, **4**, eaao3865.
- 8 C. J. Wang, K. Sim, J. Chen, H. Kim, Z. Y. Rao, Y. H. Li, W. Q. Chen, J. Z. Song, R. Verduzco and C. J. Yu, *Adv. Mater.*, 2018, **30**, 1706695.

- 9 L. Y. Zhang, L. Zhu, S. R. Larson, Y. P. Zhao and X. Q. Wang, *Soft Matter*, 2018, **14**, 4541–4550.
- 10 J. C. Ye, Y. H. An, E. Montalvo, P. G. Campbell, M. A. Worsley, I. C. Tran, Y. Y. Liu, B. C. Wood, J. Biener, H. Q. Jiang, M. Tang and Y. M. Wang, *J. Mater. Chem. A*, 2016, **4**, 4032–4043.
- 11 Z. M. Song, X. Wang, C. Lv, Y. H. An, M. B. Liang, T. Ma, D. He, Y. J. Zheng, S. Q. Huang, H. Y. Yu and H. Q. Jiang, *Sci. Rep.*, 2015, **5**, 10988.
- 12 M. Yamagami, K. M. Peters, I. Milovanovic, I. Kuang, Z. Y. Yang, N. S. Lu and K. M. Steele, *Sensors*, 2018, **18**, 1269.
- 13 Y. A. Huang, Y. J. Ding, J. Bian, Y. W. Su, J. Zhou, Y. Q. Duan and Z. P. Yin, *Nano Energy*, 2017, **40**, 432–439.
- 14 J. A. Rogers, Y. Huang, O. G. Schmidt and D. H. Gracias, *MRS Bull.*, 2016, **41**, 123–129.
- 15 T. Brugarolas, F. Q. Tu and D. Lee, *Soft Matter*, 2013, **9**, 9046–9058.
- 16 R. B. Bai and Z. G. Suo, *J. Appl. Mech.*, 2015, **82**, 071011.
- 17 Y. M. Song, Y. Xie, V. Malyarchuk, J. Xiao, I. Jung, K.-J. Choi, Z. Liu, H. Park, C. Lu, R.-H. Kim, R. Li, K. B. Crozier, Y. Huang and J. A. Rogers, *Nature*, 2013, **497**, 95–99.
- 18 L. Gao, Y. Zhang, H. Zhang, S. Doshay, X. Xie, H. Luo, D. Shah, Y. Shi, S. Xu, H. Fang, J. A. Fan, P. Nordlander, Y. Huang and J. A. Rogers, *ACS Nano*, 2015, **9**, 5968–5975.
- 19 Y. Shi, H. Y. Luo, L. Gao, C. F. Gao, J. A. Rogers, Y. G. Huang and Y. H. Zhang, *Proc. R. Soc. A*, 2015, **471**, 20150632.
- 20 L. M. Liz-Marzan, *Langmuir*, 2006, **22**, 32–41.
- 21 L. Tapaszto, G. Dobrik, P. Lambin and L. P. Biro, *Nat. Nanotechnol.*, 2008, **3**, 397–401.
- 22 Y. A. Huang, Y. Q. Duan, Y. J. Ding, N. B. Bu, Y. Q. Pan, N. S. Lu and Z. P. Yin, *Sci. Rep.*, 2014, **4**, 5949.
- 23 D. Ye, Y. J. Ding, Y. Q. Duan, J. T. Su, Z. P. Yin and Y. A. Huang, *Small*, 2018, **14**, 1703521.
- 24 J. Bian, Y. J. Ding, Y. Q. Duan, X. D. Wan and Y. A. Huang, *Soft Matter*, 2017, **13**, 7244–7254.
- 25 C. B. Williams, J. K. Cochran and D. W. Rosen, *Int. J. Adv. Des. Manuf. Technol.*, 2011, **53**, 231–239.
- 26 W. J. Arora, A. J. Nichol, H. I. Smith and G. Barbastathis, *Appl. Phys. Lett.*, 2006, **88**, 053108.
- 27 H. R. Fu, K. W. Nan, P. Froeter, W. Huang, Y. Liu, Y. Q. Wang, J. T. Wang, Z. Yan, H. W. Luan, X. G. Guo, Y. J. Zhang, C. Q. Jiang, L. M. Li, A. C. Dunn, X. L. Li, Y. G. Huang, Y. H. Zhang and J. A. Rogers, *Small*, 2017, **13**, 1700151.
- 28 C. Py, P. Reverdy, L. Doppler, J. Bico, B. Roman and C. N. Baroud, *Phys. Rev. Lett.*, 2007, **98**, 156103.
- 29 V. Flauraud, M. Mastrangeli, G. D. Bernasconi, J. Butet, D. T. L. Alexander, E. Shahrabi, O. J. F. Martin and J. Brugger, *Nat. Nanotechnol.*, 2017, **12**, 73–80.
- 30 M. Behl, M. Y. Razzaq and A. Lendlein, *Adv. Mater.*, 2010, **22**, 3388–3410.
- 31 J. P. Liu, H. Song, L. L. Zhang, H. Y. Xu and X. J. Zhao, *Macromol. Biosci.*, 2010, **10**, 1164–1170.
- 32 Y. Shi, F. Zhang, K. Nan, X. Wang, J. Wang, Y. Zhang, Y. Zhang, H. Luan, K.-C. Hwang, Y. Huang, J. A. Rogers and Y. Zhang, *Extreme Mech. Lett.*, 2017, **11**, 105–110.
- 33 S. Xu, Z. Yan, K.-I. Jang, W. Huang, H. Fu, J. Kim, Z. Wei, M. Flavin, J. Mccracken, R. Wang, A. Badea, Y. Liu, D. Xiao, G. Zhou, J. Lee, H. U. Chung, H. Cheng, W. Ren, A. Banks, X. Li, U. Paik, R. G. Nuzzo, Y. Huang, Y. Zhang and J. A. Rogers, *Science*, 2015, **347**, 154–159.
- 34 Y. H. Zhang, F. Zhang, Z. Yan, Q. Ma, X. L. Li, Y. G. Huang and J. A. Rogers, *Nat. Rev. Mater.*, 2017, **2**, 17019.
- 35 X. Guo, X. Wang, D. Ou, J. Ye, W. Pang, Y. Huang, J. A. Rogers and Y. Zhang, *npj Flex. Electron.*, 2018, **2**, 14.
- 36 F. Xu, W. Lu and Y. Zhu, *ACS Nano*, 2011, **5**, 672–678.
- 37 Y. Zhang, Z. Yan, K. Nan, D. Xiao, Y. Liu, H. Luan, H. Fu, X. Wang, Q. Yang, J. Wang, W. Ren, H. Si, F. Liu, L. Yang, H. Li, J. Wang, X. Guo, H. Luo, L. Wang, Y. Huang and J. A. Rogers, *Proc. Natl. Acad. Sci. U. S. A.*, 2015, **112**, 11757–11764.
- 38 Z. Yan, F. Zhang, J. Wang, F. Liu, X. Guo, K. Nan, Q. Lin, M. Gao, D. Xiao, Y. Shi, Y. Qiu, H. Luan, J. H. Kim, Y. Wang, H. Luo, M. Han, Y. Huang, Y. Zhang and J. A. Rogers, *Adv. Funct. Mater.*, 2016, **26**, 2629–2639.
- 39 F. Xu, X. Wang, Y. T. Zhu and Y. Zhu, *Adv. Funct. Mater.*, 2012, **22**, 1279–1283.
- 40 K. Liu and G. H. Paulino, *Proc. R. Soc. A*, 2017, **473**, 20170348.
- 41 S. Yang, E. Ng and N. Lu, *Extreme Mech. Lett.*, 2015, **2**, 37–45.
- 42 Z. Chen, W. Q. Chen and J. Z. Song, *Proc. R. Soc. A*, 2017, **473**, 20170410.
- 43 H. Cheng and J. Song, *J. Appl. Mech.*, 2014, **81**, 024501.
- 44 H. R. Fu, K. W. Nan, W. B. Bai, W. Huang, K. Bai, L. Y. Lu, C. Q. Zhou, Y. P. Liu, F. Liu, J. T. Wang, M. D. Han, Z. Yan, H. W. Luan, Y. J. Zhang, Y. T. Zhang, J. N. Zhao, X. Cheng, M. Y. Li, J. W. Lee, Y. Liu, D. N. Fang, X. L. Li, Y. G. Huang, Y. H. Zhang and J. A. Rogers, *Nat. Mater.*, 2018, **17**, 268–276.
- 45 Z. Yan, M. Han, Y. Shi, A. Badea, Y. Yang, A. Kulkarni, E. Hanson, M. Kandel, X. Wen, F. Zhang, Y. Luo, Q. Lin, H. Zhang, X. Guo, Y. Huang, K. Nan, S. Jia, A. W. Oraham, M. B. Mevis, J. Lim, X. Guo, M. Gao, W. Ryu, K. J. Yu, B. G. Nicolau, A. L. Petronico, S. Rubakhin, J. Lou, P. M. Ajayan, K. Thornton, G. Popescu, D. Fang, J. V. Sweedler, P. V. Braun, H. Zhang, R. G. Nuzzo, Y. Huang, Y. Zhang and J. A. Rogers, *Proc. Natl. Acad. Sci. U. S. A.*, 2017, **114**, E9455–E9464.
- 46 Y. Su, J. Wu, Z. Fan, K.-C. Hwang, J. Song, Y. Huang and J. A. Rogers, *J. Mech. Phys. Solids*, 2012, **60**, 487–508.
- 47 J. Song, H. Jiang, Z. J. Liu, D. Y. Khang, Y. Huang, J. A. Rogers, C. Lu and C. G. Koh, *Int. J. Solids Struct.*, 2008, **45**, 3107–3121.
- 48 Y. Liu, Z. Yan, Q. Lin, X. L. Guo, M. D. Han, K. Nan, K. C. Hwang, Y. G. Huang, Y. H. Zhang and J. A. Rogers, *Adv. Funct. Mater.*, 2016, **26**, 2909–2918.
- 49 Z. C. Fan, K. C. Hwang, J. A. Rogers, Y. G. Huang and Y. H. Zhang, *J. Mech. Phys. Solids*, 2018, **111**, 215–238.
- 50 H. Y. Cheng and S. D. Wang, *J. Appl. Mech.*, 2014, **81**, 044501.